Neutral thermospheric dynamics observed with two scanning Doppler imagers: 1. Monostatic and bistatic winds

C. Anderson,[1] M. Conde,[1] and M. G. McHarg[2]

Received 28 July 2011; revised 13 October 2011; accepted 30 December 2011; published 6 March 2012.

[1] Doppler-shift measurements of the thermospheric 630.0 nm emission recorded by two spatially separated imaging Fabry-Perot spectrometers in Alaska have been combined to infer F region horizontal wind vectors at approximately 75 locations across their overlapping fields-of-view. These "bistatic" horizontal wind estimates rely only on an assumption regarding the local vertical wind (and assume a common observing volume), and thus represent a more direct measurement of the wind than do the monostatic (single-station) vector wind fields routinely inferred by these instruments. Here we present comparisons between both the independently derived monostatic wind fields from each instrument and the bistatic wind estimates inferred in their common observing volumes. Data are presented from observations on three nights during 2010. Two principal findings have emerged from this study. First, the monostatic technique was found to be capable of estimating the actual large-scale wind field reliably under a large range of geophysical conditions, and is well suited to applications requiring only a large-scale, 'big picture' approximation of the wind flow. Secondly, the bistatic (or tristatic) technique is essential for applications requiring detailed knowledge of the small-scale behavior of the wind, as for example is required when searching for gravity waves.

Citation: Anderson, C., M. Conde, and M. G. McHarg (2012), Neutral thermospheric dynamics observed with two scanning Doppler imagers: 1. Monostatic and bistatic winds, *J. Geophys. Res.*, *117*, A03304, doi:10.1029/2011JA017041.

1. Introduction

[2] High-resolution Doppler spectra of narrow-band optical emissions from Earth's thermosphere have been used since the 1960's for remote sensing of wind and temperature fields at the heights where these emissions originate [e.g., *Wark*, 1960; *Jarrett and Hoey*, 1966; *Roble et al.*, 1968]. Two particularly useful emissions are due to transitions from the ^1S and ^1D states of atomic oxygen, corresponding to wavelengths of 557.7 nm and 630.0 nm respectively. However typical Doppler spectral widths of these lines are only of order 10^{-12} m, and typical Doppler shifts of order 10^{-13} m. The technique thus requires very high spectral resolution and stability. Because of this, and the need to observe the weak emissions with maximum possible optical throughput, Fabry-Perot spectrometers have long been the preferred instrument for this application.

[3] Recently, instruments have been deployed which combine all-sky fore-optics with separation-scanned Fabry-Perot etalons to enable measurement of spectral line profiles of upper-atmospheric optical emissions from many tens of locations across the sky, simultaneously [*Conde and Smith*, 1997, 1998; *Griffin et al.*, 2008; *Anderson et al.*, 2009; *Aruliah et al.*, 2010]. These scanning Doppler imagers (SDI's) have the distinct advantage of sampling the wind field at many tens of locations simultaneously, and are thus able to resolve horizontal spatial structures at high resolution (down to scales of around 100 km or less when observing the 630.0 nm line) without serious distortion due to temporal variation of the wind field.

[4] The usual technique to infer horizontal vector wind fields from single-station (monostatic) SDI measurements (outlined in section 3.2) relies on assumptions about the functional form of the spatial wind variation (a first-order Taylor approximation) and requires an additional *a priori* constraint on one of the partial derivatives in the Taylor expansion. The validity of these assumptions has usually been difficult to ascertain, due to a lack of independent data sets providing the same spatial and temporal resolution with which to compare the horizontal wind fields inferred from these instruments.

[5] It is possible to reduce the number of assumptions required to estimate horizontal wind vectors by measuring wind components in a given sky volume along more than one line-of-sight. Such observations are generally termed bistatic or tristatic, depending on whether two or three independent lines-of-sight are used. For example, *Sipler et al.* [1995] used bistatic Fabry-Perot interferometer (FPI)

[1]Geophysical Institute, University of Alaska Fairbanks, Fairbanks Alaska, USA.
[2]Physics Department, U.S. Air Force Academy, Colorado Springs, Colorado, USA.

0148-0227/12/2011JA017041

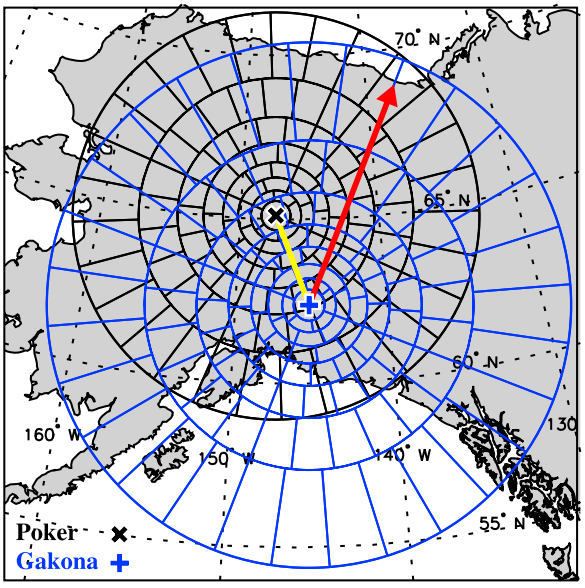

Figure 1. Gakona (blue) and Poker Flat (black) zone maps, projected onto a fixed altitude of 240 km above Alaska. The yellow line shows the Gakona/Poker Flat great circle, while the red arrow indicates the direction perpendicular to the auroral oval at 240 km altitude (and interpreted here as geomagnetic north).

measurements to infer thermospheric midlatitude vertical winds at off-zenith locations, while *Aruliah et al.* [2004, 2005] used tristatic FPI measurements and collocated tristatic radar measurements to demonstrate the meso-scale behavior of thermospheric winds and temperatures and to infer the contribution of the neutral wind dynamo to the Joule heating rate. Bistatic and tristatic data were used by *Ford et al.* [2006, 2008] to study thermospheric gravity waves, and *Meriwether et al.* [2006] have discussed a tristatic Fabry-Perot interferometer array in Alaska. Recently, auroral zone thermospheric vertical winds have been investigated by combining SDI and narrow-field FPI measurements above Antarctica [*Anderson et al.*, 2011].

[6] The Geophysical Institute has operated a SDI at Poker Flat since 1994 [*Conde and Smith*, 1995]. In 2009, a second SDI owned by the US Air Force Academy was deployed to Gakona. The close proximity of these two instruments (refer to Figure 1) guarantees a significant amount of overlap between the instrument fields-of-view (∼90% and ∼60% respectively of the Poker Flat and Gakona fields-of-view overlap). We are therefore able, for the first time, to compare horizontal wind maps independently estimated by two SDI's viewing a common-volume. More importantly, the geometry afforded by the two instruments allows for bistatic sampling of the wind field at many points (typically several tens) in the combined field-of-view. Inversion of these bistatic samples provides a direct measurement of two components of the three-component wind vector at each bistatic location, which, when combined with any reasonable assumption about the vertical wind field (in addition to the assumption of a common-volume, as discussed in section 3.3), can be resolved into horizontal wind vectors and compared directly with the monostatic wind maps generated independently by each instrument.

[7] This paper is the first of three investigating F-region thermospheric dynamics in the auroral zone, as observed by the two SDI's currently operating at Poker Flat and Gakona, in Alaska. The current article provides details on the instruments themselves and the analysis schemes used to derive both monostatic (i.e. single-station) vector wind fields and bistatic common-volume winds. We also present results comparing concurrent monostatic wind estimates from both instruments with the bistatic winds derived from their combined measurements. A second paper will focus on the behavior of the vertical winds recorded both in the station zeniths and at locations along the great circle between them, and a third will present an investigation into the behavior of the horizontal wind gradients inferred from the bistatic winds.

2. Instrumentation

[8] In this work, data are presented from the two scanning Doppler imagers (SDI's) located at Poker Flat (65.12N, 147.43W) and Gakona (62.39N, 145.15W), in Alaska (local time = UT − 9, magnetic local time ≃ UT + 12.8). These instruments are identical in concept, although they differ in design. The operational principles governing these instruments have been described by *Conde and Smith* [1997]. Briefly, a fish-eye lens is used to accept light from a large (∼75° or greater) half-angle field-of-view of the sky. This light passes first through a narrowband interference filter, and then through a wide-aperture, capacitance-stabilized Fabry-Perot etalon. Piezoelectric ceramics between the etalon plates allow the etalon gap to be scanned in separation over one order of interference. Skylight, modulated by the concentric circular interference fringe pattern due to the etalon, is then imaged onto a thermoelectrically cooled, electron-multiplying CCD (EMCCD) camera.

[9] An individual etalon scan is achieved by varying the etalon plate separation over one order of interference in N discrete steps (or 'channels'). For the current work $N = 128$ for both instruments. A fringe-modulated sky image is recorded by the camera at each step, with a typical integration time per step of 0.18 s (this value is configurable, from around 0.1 s up to arbitrarily long times). For the purpose of spectral accumulation the imaging area of the CCD is subdivided in software into a number of regions called 'zones', which define contiguous sets of pixels. Data for pixels comprising a given zone are combined to produce a single recorded sky spectrum. The control software internally maintains two look-up tables which are used at each step in the scan to determine a) to which spectrum a given pixel contributes (or, equivalently, to which zone it belongs), and b) the offset applied to the current scan channel in order to determine which spectral channel will receive the digital number recorded at the given pixel. The first of these tables is called a 'zone map', and essentially maps pixel location on the EMCCD detector (and hence sky observing volume) to zone number. The second table is required to compensate for the variation of interference order within a zone, as described by *Conde and Smith* [1997], and is called a 'phase map'. Only one of each look-up table is required by this technique.

[10] Together, the zone map and phase map allow independent spectra to be simultaneously accumulated from as

many regions of the sky as there are zones defined. There is an inherent trade-off between spatial resolution (fixed by the number and size of the zones) and temporal resolution, since larger zones intercept more light per unit time, but use more of the detector's available pixels. For the present work both instruments were configured to use 115 zones, formed from annular segments (and a circular central zone), as shown in Figure 1. In this figure the Gakona and Poker Flat zone maps are shown projected onto an altitude of 240 km. The Poker flat field-of-view does not extend as far in zenith angle as that of the Gakona SDI, and thereby maps to a smaller area on the sky. Geomagnetic north (more correctly the direction perpendicular to the auroral oval at 240 km altitude) is indicated by the red arrow, and the Gakona/Poker Flat great circle is shown by the yellow line. It is evident from the figure that there is substantial overlap between the two fields-of-view, thus these instruments are well situated for bistatic observations.

[11] Spectra from multiple etalon scans are co-added to form a single 'exposure'. Co-adding multiple rapid scans limits possible spectral distortion due to temporal variation in brightness. A single scan takes on average ~23 seconds, and the number of co-added scans per exposure is dynamically adjusted by the control software to enforce a minimum median spectral signal-to-noise ratio across all zones. The number of scans per exposure ranges from a forced minimum of four scans under active conditions of bright aurora to 26 scans during quiet conditions (corresponding to a maximum exposure time of 10 minutes). Henceforth the central time of the exposure (the mean of the exposure start and end times) will be used when discussing the time at which an exposure was made (from either instrument).

3. Analysis

3.1. Spectral Fitting and Drift Removal

[12] The basic data recorded by the SDI during a single exposure are sky spectra spanning approximately 10 pm, one spectrum in each zone. For calibration each instrument routinely observed the light from a frequency-stabilized He-Ne laser source. The recorded laser profiles provided a direct measurement of the instrument function, and were used to extract geophysical information from the recorded airglow profiles, using the algorithm described by *Conde* [2001], adapted to work with passive FPI spectra. The algorithm generated estimates of peak wavelength (relative to the calibration source peak wavelength), temperature, emission and continuum intensity, by least squares fitting a model Gaussian emission profile (convolved with the measured instrument function) to the observed airglow spectra.

[13] Dummy emission profiles were also fitted to the calibration spectra in order to track the inferred peak wavelength of the calibration source (the wavelength of which was assumed constant). Airglow peak wavelengths were corrected for instrumental drift by applying a high-pass polynomial filter to the measured calibration peak wavelengths, and thereby rejecting features in the measured airglow Doppler time series with periods greater than approximately 2–3 hours. Line-of-sight velocities were then derived by referencing the drift-corrected peak wavelengths to an assumed zero velocity reference. For this work the zero velocity reference was calculated by assuming that the mean zenith-looking peak wavelength over an entire night corresponded to the 630.0 nm rest wavelength, or equivalently that the net vertical wind velocity over an entire night was 0 ms^{-1}. This is a commonly used assumption in the absence of a convenient laboratory source at 630.0 nm (for a discussion of this assumption, see *Aruliah and Rees* [1995]).

3.2. Monostatic Wind Fit

[14] The procedure for fitting a two-dimensional horizontal vector wind field to a set of azimuthal line-of-sight wind samples has been described by *Conde and Smith* [1998]. This method is based on earlier work by *Browning and Wexler* [1968], and was first applied to neutral wind measurements by *Burnside et al.* [1981]. For full details on the present application of this technique the reader is referred to *Conde and Smith* [1998], however a brief description is provided here.

[15] The horizontal wind field is modeled by a first-order Taylor expansion about the station zenith, with zonal u and meridional v components given by

$$u = u_0 + \frac{\partial u}{\partial x}x + \frac{\partial u}{\partial y}y \tag{1}$$

$$v = v_0 + \frac{\partial v}{\partial x}x + \frac{\partial v}{\partial y}y \tag{2}$$

where u_0 and v_0 are the uniform zonal and meridional wind components respectively, and the partial derivatives are taken with respect to the zonal x and meridional y horizontal distances.

[16] The basic 'data unit' for the monostatic wind fit is a set of line-of-sight wind measurements at a constant zenith angle. Thus the set of (drift-corrected) line-of-sight wind estimates within an annulus of zones forms the data unit for the current work, from which are estimated the uniform wind and gradient terms in the Taylor expansion. Assuming a uniform vertical wind field, the contribution to the line-of-sight wind from a vertical wind V_z is constant around an annulus, and equal to $V_z\cos(\phi)$ for a given zenith angle ϕ. The vertical wind measured in the station zenith can then be used to remove the vertical wind contribution from all line-of-sight samples. This yields a set of horizontal line-of-sight wind estimates as a function of observation azimuth.

[17] The azimuthal wind variation is then represented by a discrete Fourier series, and the Fourier coefficients for this series calculated. For all data presented here the number of azimuthal samples in any given annulus (excluding the central zone) was always ≥6, which allowed the Fourier coefficients describing the mean, fundamental and first harmonic variations to be calculated in each annulus (five unique coefficients). These Fourier coefficients are related [see, e.g., *Browning and Wexler*, 1968; *Burnside et al.*, 1981] to the coefficients of the Taylor expansion (the uniform wind and gradients terms in equations (1) and (2)). Two of the Fourier coefficients relate directly to the uniform wind terms u_0 and v_0. Three equations then relate the remaining three Fourier coefficients to the four partial derivatives of the Taylor expansion. In order to solve this system of equations an additional constraint on one of the four partial derivatives is required.

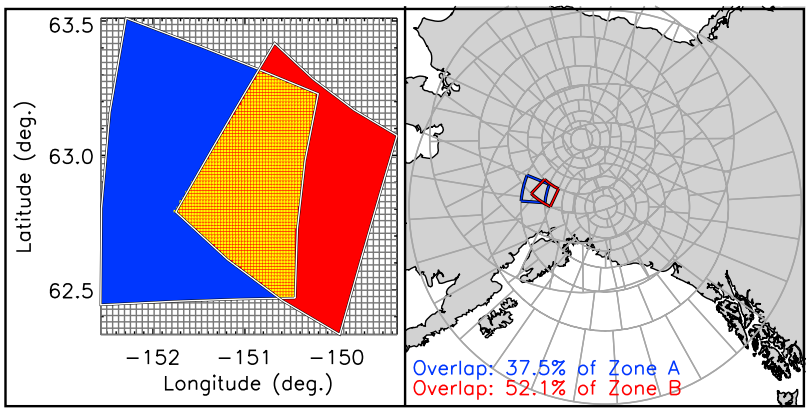

Figure 2. Calculating the percentage zone overlap. (left) A Gakona (zone A, blue) and Poker Flat (zone B, red) zone pair, after discretization (the grid lines show the grid at half the available resolution). The calculated overlap region is indicated by the yellow region. (right) The locations of the given zones with respect to the instrument zone maps and the calculated percentage of each zone's area, which is common to both zones.

[18] *Burnside et al.* [1981] relied on the assumption of a wind field that was stationary in local time, thus allowing an estimate of the zonal gradient of the meridional wind (the $\partial v/\partial x$ term in equation (2)) to be made from time-consecutive measurements of the meridional wind. *Conde and Smith* [1998] considered the validity of this assumption in the auroral zone, and pointed out that the $\partial v/\partial x$ term calculated in this way was often small compared to both the uniform wind and the other three spatial gradients. However, when the local wind field is rapidly time-varying, as for example can occur during substorms, wind fields derived under this assumption can often be unrealistic. Considerable experience has shown that setting $\partial v/\partial x = 0$ (in geomagnetic coordinates) produces wind fields which are reasonable under both steady/quiet and dynamic conditions, and this assumption has been used in the current work. Gradients inferred independently from bistatic data (including $\partial v/\partial x$) will be investigated in a future paper.

[19] Once the uniform wind and partial derivatives are calculated within each annulus, a final estimate of the horizontal wind at each observing location is calculated by combining the measured horizontal (radial) line-of-sight wind estimate at that location with the component of the modeled wind perpendicular to the line-of-sight. That is, for each viewing zone, the fitted coefficients of the Taylor expansion are used to calculate a modeled horizontal wind normal to the line-of-sight, and this is combined with the directly measured radial component of the horizontal wind at that location in order to produce a total horizontal wind vector. In this way the full variability present in the measured line-of-sight data is preserved, and only the perpendicular component is modeled.

3.3. Bistatic Wind Fit

[20] Where two wind estimates are obtained from the same (approximate) observing volume along two different lines-of-sight, they can be used to uniquely resolve two of the three components of the true wind vector in the common-volume, specifically those components lying in the plane formed by the two observatories and the given common-volume point. From Figure 1 it is obvious that there were a significant number of overlapping zones between the Poker Flat and Gakona SDI's. The first step in making use of these common-volume observations was that of quantifying the degree of overlap between each of the Poker-Gakona zone pairs, in order to identify candidate wind estimate pairs for bistatic inversion.

[21] The approach used here was to consider all possible Poker-Gakona zone pairs, a total of 13225 pairs in all. For each pair of zones, the following steps were performed (see Figure 2). First, the outline of each zone was approximated by a polygon containing n vertices, where $n \geq 4$ was configurable but here set equal to 12 (the polygon was needed to make a reasonable approximation of the two curved boundaries of a zone). The geographical projection (latitude and longitude) of each vertex in each zone was then calculated using an assumed altitude of 240 km. From these the minimal latitude and longitude range required to contain both approximate zone outlines was determined, and these ranges used to construct a 100 × 100 pixel grid of points which were either interior or exterior to each zone (a value of 1 or 0 respectively in the discrete grid).

[22] Denoting the value of the grid cell at location (x, y) by $c(x, y)$, the set:

$$U_i = \{c_i(x,y) \text{ such that } c_i(x,y) = 1, x, y \in [0, 99]\} \quad (3)$$

defined the interior of the discretized zone, where the braces $\{\}$ are used to enumerate the set elements and $i \in [1, 2]$ indicates which of the two zones in the pair are being considered. Since both zones were discretized onto the same grid, the overlap set O was found by simple comparison:

$$O = U_1 \cap U_2 \quad (4)$$

The quantities of interest were the fraction of each zone's total area which was contained in the region of overlap, thus

$$o_i = \frac{|O|}{|U_i|} = \frac{|U_1 \cap U_2|}{|U_i|} \quad (5)$$

where for a given set S, the notation S denotes the number of elements contained in S (the 'cardinality' of the set). The end

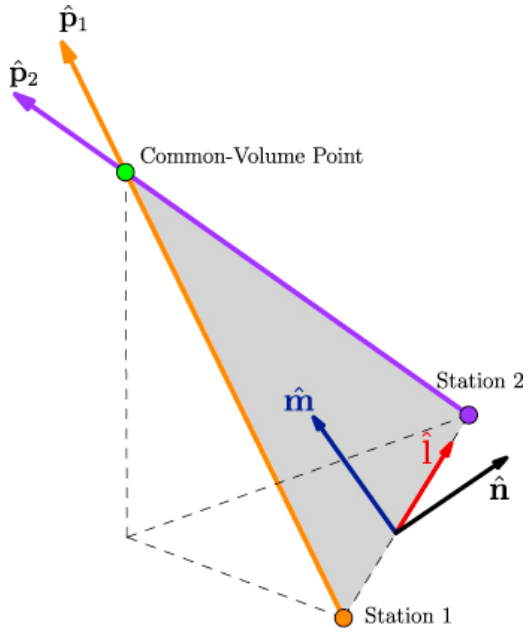

Figure 3. Bistatic geometry. Lines-of-sight ($\hat{\mathbf{p}}_i$) from each station to a common-volume location (green dot) are shown by orange and purple arrows. The 'viewing-plane' formed by the $\hat{\mathbf{p}}_i$'s is shown by the grey shaded region. Viewing-plane coordinate axes ($\hat{\mathbf{l}}$, $\hat{\mathbf{m}}$, $\hat{\mathbf{n}}$) are also depicted.

result of the above procedure was two numbers $(o_1, o_2) \in [0, 1]$ for every Poker-Gakona zone pair, quantifying the fraction of each zone's total area that was contained within the other zone in the pair. The maximum of these two fractions, $\max(o_1, o_2)$, was then used to filter out zone pairs which did not satisfy the desired amount of overlap. The maximum value was used because, for example, a small zone may be completely contained within a larger zone, in which case $\max(o_1, o_2) = 1$, while $\min(o_1, o_2)$ could possibly be much less than 1. For this work the minimum degree of overlap was set to 10%, which translated to the condition $\max(o_1, o_2) \geq 0.1$. Although this might appear to be a weak overlap criterion, in practice it ensured a median overlap of ~43%. Experience with the analysis showed that the final results were not strongly affected by the details of this procedure.

[23] Once bistatic zone-pairs had been identified, inversion of the two line-of-sight wind estimates in each pair was achieved as follows. A common-volume location was assigned by finding the halfway point between the centers of the overlapping zones (the actual assigned location does not strongly influence the results). Let the unit vector along the line-of-sight from station s_i to the common-volume point be denoted by $\hat{\mathbf{p}}_i$. The two vectors $\hat{\mathbf{p}}_i$ define a plane whose normal is $\hat{\mathbf{n}} = (\hat{\mathbf{p}}_1 \times \hat{\mathbf{p}}_2)/(|\hat{\mathbf{p}}_1 \times \hat{\mathbf{p}}_2|)$ (refer to Figure 3). The resultant wind vector is completely resolved in this plane, while the component along $\hat{\mathbf{n}}$ is wholly unknown. The first step in the inversion is to define a new coordinate system in the plane defined by $\hat{\mathbf{n}}$ (the 'viewing-plane'), onto which the line-of-sight wind estimates can be projected. A convenient choice is to use the unit vector in the direction from the lower to the higher-latitude station, denoted $\hat{\mathbf{l}}$. An orthogonal axis $\hat{\mathbf{m}}$ is then obtained by rotating $\hat{\mathbf{l}}$ by 90° around the $\hat{\mathbf{n}}$ direction, which produces a right-handed coordinate system.

[24] Neglecting measurement uncertainty, the true wind vector $\mathbf{r}$ at the common-volume location is related to the measured line-of-sight wind estimates d_i by

$$d_i = \hat{\mathbf{p}}_i \cdot \mathbf{r} \tag{6}$$

or in matrix notation

$$\mathbf{d} = \mathbf{P}\mathbf{r} \tag{7}$$

where the rows of $\mathbf{P}$ are made up of the individual $\hat{\mathbf{p}}_i$'s. By transforming to viewing-plane coordinates (defined by the $\hat{\mathbf{l}}$ and $\hat{\mathbf{m}}$ axes), the 2×3 matrix $\mathbf{P}$ of equation (7) becomes a square (2×2) matrix, and the equation can then be solved uniquely for the components of $\mathbf{r}$ in the viewing-plane by inverting $\mathbf{P}$ and calculating $\mathbf{r}$ using the following

$$\begin{pmatrix} r_l \\ r_m \end{pmatrix} = \begin{pmatrix} \hat{\mathbf{p}}_1 \cdot \hat{\mathbf{l}} & \hat{\mathbf{p}}_1 \cdot \hat{\mathbf{m}} \\ \hat{\mathbf{p}}_2 \cdot \hat{\mathbf{l}} & \hat{\mathbf{p}}_2 \cdot \hat{\mathbf{m}} \end{pmatrix}^{-1} \begin{pmatrix} d_1 \\ d_2 \end{pmatrix} \tag{8}$$

where the first term on the right-hand-side is the inverse of $\mathbf{P}$.

[25] For the purposes of inversion, all vector components were calculated relative to a Euclidian coordinate basis with origin at Earth's center. Resultant wind vectors were then transformed back into the local coordinate system (relative to unit vectors in the zonal, meridional and zenith directions) as needed by assuming a value for the local vertical wind. The quality of the inversion depends both upon the quality of the underlying wind estimates and on the geometry of the lines-of-sight. Intuitively, as the dot product $\hat{\mathbf{p}}_1 \cdot \hat{\mathbf{p}}_2$ increases, the less tolerant the inversion becomes to noise in the data (the system becomes ill-conditioned). The quantity $\chi = \hat{\mathbf{p}}_1 \cdot \hat{\mathbf{p}}_2$ was therefore one parameter used to assess the stability of the inversion. A second useful quantity for classifying the bistatic geometry was the angle between the viewing-plane normal and the local (to the common-volume) vertical. This quantity, given by

$$\eta = \cos^{-1}(\hat{\mathbf{n}} \cdot \hat{\mathbf{z}}) \tag{9}$$

where $\hat{\mathbf{z}}$ is the unit vector in the local zenith direction, measured the degree to which an observing volume was off-zenith. Thus for small η the resolved wind component r_m was essentially the vertical wind. Other indicators which were used to assess/filter the bistatic wind fits were the absolute and fractional uncertainty in the $\hat{\mathbf{l}}$ and $\hat{\mathbf{m}}$ wind components (due to the uncertainties in the underlying line-of-sight wind estimates and the geometry of the bistatic location) and the maximum percentage overlap of the zones used for the inversion. The effect of geometrical filtering (that is, filtering by zone overlap, η and χ) is shown in Figure 4. Note the band of locations close to the Poker-Gakona great circle which were rejected based on η.

[26] The basic data unit for the bistatic inversion at any given time was two sets of line-of-sight wind estimates, one set from each of the Poker Flat and Gakona SDI's. Since the exposures from each instrument were not synchronized in time, an interpolation scheme was used to produce

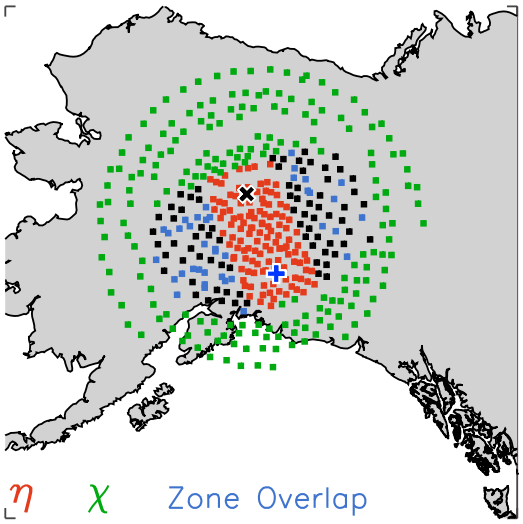

Figure 4. Geometrical filtering of bistatic locations. Colored squares indicate bistatic locations that have been rejected based on geometrical criteria: zone overlap (blue), η (red), χ (green). Black squares indicate locations accepted for further processing (and possible filtering by wind uncertainty). Where a location was rejected based on more than one of the above criteria, colors were assigned with the following precedence: χ rejection, η rejection, zone overlap rejection.

concurrent wind estimates at a set of 'common' times, defined by the union of the sets of observation times from each instrument. Thus at a given common time, if measured data were available from instrument A, data from instrument B were linearly interpolated to that time, and vice versa. In this article, where interpolated data at a given common time were separated by more than five minutes from a direct measurement, this common time was rejected from further analysis/display. Thus for all data presented here the bistatic wind estimates were derived from one set of direct and one set of temporally interpolated wind measurements, where the interpolated wind measurements were separated by less than five minutes from a direct measurement.

[27] A basic assumption here is that the two instruments act as an array, observing the same underlying geophysical fields, at the same fixed altitude, but from two different perspectives. A useful diagnostic of the validity of this assumption is the degree of correlation between the (scalar) intensity and temperature measurements made by each instrument in zones that have been identified as overlapping. Such a comparison is shown in Figure 5 (left), where time series data from the night of April 2, 2010 are shown in three common-volume regions. Each row in this figure shows a different Gakona/Poker Flat zone pair, indicated by text above the row. Columns show intensity (left) and five-minute smoothed temperature (right) comparisons throughout the night between the Gakona (blue curve) and Poker Flat (black curve) instruments. These instruments are not calibrated for absolute intensity measurements (in Rayleigh

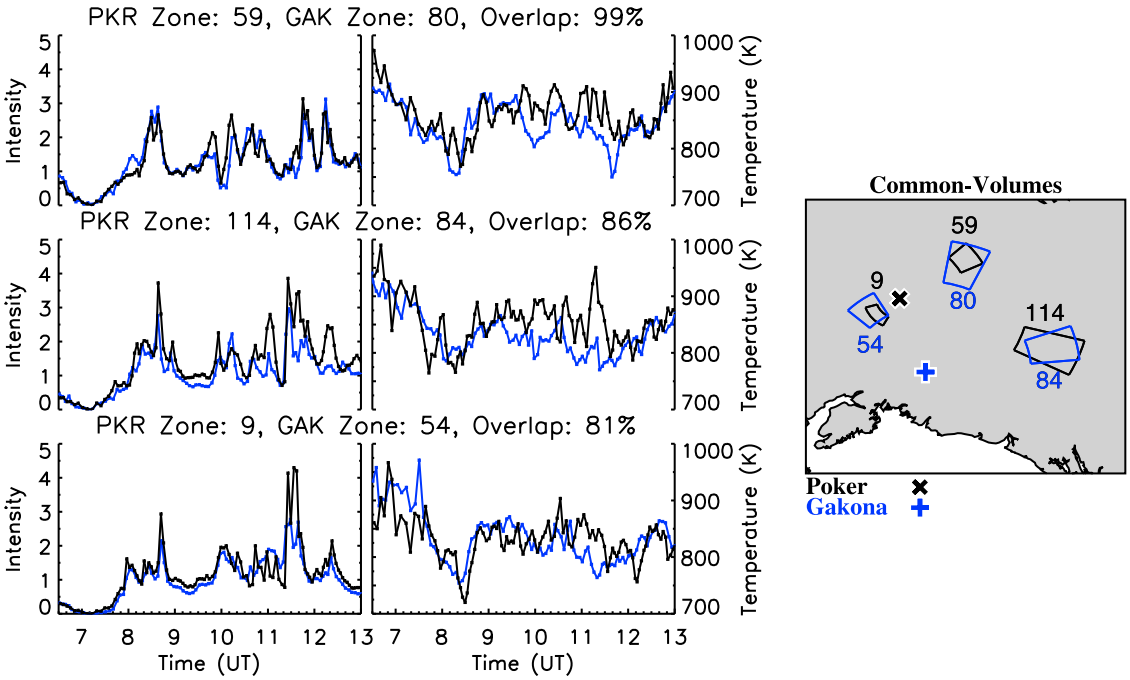

Figure 5. (left) Time series of intensity (left column) and five-minute smoothed temperature (right column) estimates from each station (Poker Flat, black; Gakona, blue) in three different common-volume regions. The zone numbers of the common-volumes and the percentage overlap between the Poker and Gakona zones (as described in the text) are indicated above each row. Intensities from the Gakona SDI have been multiplied by 35 to aid comparison between the uncalibrated intensity measurements, and measurement uncertainties are omitted for clarity. Data are from April 2, 2010. The map to the right shows the locations of the zones in which these data were recorded.

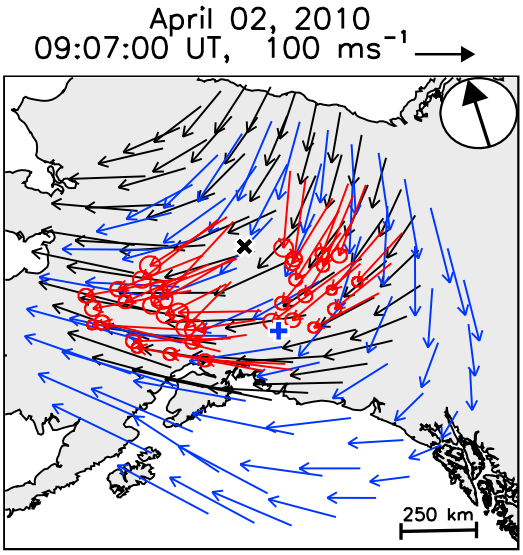

Figure 6. Example wind field comparing monostatic fields from Poker Flat (black) and Gakona (blue) with the bistatic winds (red) derived using line-of-sight data from each station in the common-volume regions. Red circles indicate uncertainties for the bistatic wind vectors. The arrow in the circle (top right corner) indicates the sunward direction. The date and universal times at which the Poker Flat and Gakona exposures were recorded are shown at the top of the figure.

for example), and thus in Figure 5 the raw intensities measured by the Gakona SDI have been multiplied by 35 to aid comparison. The common-volumes in which these data were recorded are shown in the map on the right of Figure 5.

[28] Since each measurement represents an emission intensity-weighted integral along a unique line-of-sight, some discrepancy between the estimates from each instrument is to be expected in addition to measurement noise. However, the high degree of correlation between the two sets of measurements indicate that on this night, and at these locations, the two instruments were indeed viewing a common-volume, and conditions were such that the bistatic wind inversion would be expected to produce reliable wind estimates.

[29] For the example data shown in Figure 5, the linear Pearson correlation coefficient (over the entire time range) between the intensity estimates from each instrument were (top to bottom row) 0.91, 0.88 and 0.88. The temperature correlation was 0.63, 0.53 and 0.60, which are lower than the intensity coefficients due to greater noise as a result of larger fractional measurement uncertainties (approximately 4% for temperature compared with 1% for intensity). The likelihood of attaining these levels of correlation purely by chance is negligible (less than 1 in 10^9 for the worst of these coefficients).

[30] The plots shown in Figure 5 are typical examples of the data that have been analyzed thus far. However, note that comparisons of emission intensity and temperature measurements in overlapping zones can only be used to give a qualitative indication of the degree to which two volumes were 'common'. The nature of the thermospheric temperature field is such that even non-overlapping zones may produce well-correlated temperature estimates, and conversely zones that very closely overlap may produce poorly correlated intensity estimates due to different lines of sight and the three-dimensional structure of the aurora. Comparisons between intensity and temperature estimates of the type shown in Figure 5 were used only as an approximate check on the validity of the common-volume assumptions, and correlation coefficients were not used in a quantitative way to select common-volumes for bistatic inversion.

[31] An example comparison of monostatic and bistatic wind estimates is shown in Figure 6, also for measurements taken on April 2, 2010. This figure serves to introduce the plot format which will be adopted for subsequent figures. The universal time at the top of the panel indicates the average of the times at which each instrument recorded the given exposure. The arrow in the top right corner of the figure indicates the sunward direction. Rotating a given map until this arrow points vertically upward (toward the top of the page) will give the map the same orientation as it would have if it were placed on a dial-type plot in geomagnetic coordinates [e.g., *Conde and Smith*, 1998, Figure 2], in the appropriate magnetic local time sector. This visualization allows the observed wind flows to be placed in the context of the large-scale ionospheric convection pattern.

[32] Monostatically derived wind fields from Poker Flat and Gakona are shown by black and blue arrows respectively. Each instrument recorded line-of-sight wind estimates at 115 locations across the sky, and these estimates did not cover the geographically projected field-of-view evenly (the zone maps in Figure 1 makes this obvious). Thus the monostatic data from both stations were first interpolated onto an even spatial grid, and then sub-sampled to reduce the number of displayed vectors to 65 per station.

[33] Bistatic wind vectors derived from the line-of-sight wind estimates in the common-volume regions are shown in red, along with circles representing the uncertainties in these vectors (derived from the uncertainties in each of the $\hat{\mathbf{l}}$ and $\hat{\mathbf{m}}$ wind components). These data were pre-filtered by requiring that $\max(o_1, o_2) \geq 0.1$, $\chi < 0.82$, $\eta > \pi/6$, and that the individual wind component absolute (relative) uncertainties were less than 40 ms^{-1} (40%). The horizontal projection of the bistatic winds was achieved by assuming a zero vertical wind. The effect of using a non-zero vertical wind for this projection is to introduce a rotation of the bistatic wind vectors, the sense of which is opposite on opposite sides of the Gakona/Poker Flat great circle. The magnitude of the rotation depends on η, and given the relatively large zenith angles of the filtered bistatic data ($\eta > \pi/6$), the vertical wind assumption does not have a noticeable impact on the wind results reported here, for typical vertical wind magnitudes of $\leq$30 ms^{-1} [e.g., *Conde and Dyson*, 1995; *Greet et al.*, 2002].

[34] In the particular example shown in Figure 6 the monostatically derived wind fields from each station were in very close agreement with each other. The spatial coverage of the filtered bistatic winds was good, and the horizontal projections of the bistatic winds were also in close agreement with the monostatic wind fields. While bistatic spatial coverage was not always as good as that shown in Figure 6 due to data rejection based on wind component uncertainties (data rejection based on viewing geometry of course remained constant with time), the monostatically derived

wind fields very often gave consistent estimates of the wind flow above Alaska, and these estimates were strongly reinforced by the bistatic data where available.

4. Results

[35] The bistatic analysis described above has been performed on 19 days from 2010. Here we present results from three of those days to demonstrate some of the more interesting behavior that was observed. The wind fields inferred on these nights were not atypical. The non-uniform wind flows shown here were commonly observed on other nights as well, with similar structure. For each night presented, bistatic results have been filtered as described for the example data in Figure 6. Geometrical filtering (requiring $\max(o_1, o_2) \geq 0.1$, $\chi < 0.82$, $\eta > \pi/6$) reduced the maximum number of potential bistatic data points to 75. These were further filtered in each exposure by rejecting bistatic winds with an absolute (relative) uncertainty in either of the wind components ($\hat{\mathbf{l}}$ or $\hat{\mathbf{m}}$) of greater than 40 ms^{-1} (40%). Bistatic wind uncertainties have been omitted in the following figures to improve clarity. See Figure 6 for the typical spatial variation of the bistatic wind uncertainty.

4.1. January 24, 2010

[36] Data from January 24, 2010 are shown in Figure 7. These data span most of the night and are displayed at a nominal time resolution of 45 min (very much lower than the time resolution of the original data). Wind flow at 0500 UT was predominantly antisunward (the sunward direction is indicated by the arrow in the top right corner of each panel). Sunward wind flow was observed to develop in the magnetic north beginning around 0600 UT. By 0730 UT the sunward flow was well established in the magnetic north, while antisunward flow persisted south of Gakona. Thus this wind field had developed strong magnetic latitudinal shear. Between 0645 and 0905 UT only bistatic data magnetically north of the Gakona/Poker Flat great circle met the filtering criteria. During this time period the monostatic wind estimates showed sunward flow of 200–300 ms^{-1} in the magnetic north, and the collocated bistatic wind estimates were in good agreement with the monostatic estimates in both direction and magnitude.

[37] From 0952 UT onwards the coverage of the filtered bistatic data improved to the point where approximately equal numbers of bistatic data points were retained on both sides of the Gakona/Poker Flat great circle by 1037 UT. At 0952 UT the flow magnetically south and southeast of Gakona had decreased in magnitude and no longer showed a spatially consistent direction. The beginnings of magnetic equatorward flow were observed in the magnetic east at 1037 UT. Curvature was also observed in the wind field at this time, with magnetic southward/southwestward flow in the magnetic north, changing to magnetic westward flow in the magnetic southwest, possibly associated with the edge of the duskside ionospheric convection cell. This curvature was observed in both the monostatic and bistatic wind estimates.

[38] By 1125 UT (close to magnetic midnight) a magnetic westward component was still present in the winds to the magnetic west, while southward flow was observed to the east. Divergent flow was apparent at 1210 UT, with antisunward flow in the magnetic south and southwest, and southeastward flow in the magnetic north and east. A similar large-scale flow pattern was present in the final displayed frame at 1343 UT, however by this time antisunward flow had also developed along the magnetic south and southeast edges of the Gakona field-of-view.

[39] This night displayed characteristics which are very commonly observed above Alaska. For example sunward flow in the magnetic north in the magnetic dusk sector, associated with meridional shear, antisunward flow near magnetic midnight (~1130 UT) and divergence associated (presumably) with the divergent ionospheric convection in the magnetic midnight sector, and generally antisunward or equatorward flow in the magnetic dawn sector. Both SDI's on this night inferred consistent wind fields at both large (~1000 km) and small (~100 km) scales, and these fields were in good agreement with the bistatic wind estimates (which were projected on to the horizontal by assuming zero vertical wind).

[40] Further corroboration of the inferred wind flow on this night comes from a comparison with measurements made by independent Fabry-Perot interferometers located at Fort Yukon and Poker Flat (J. Meriwether, personal communication, 2011). Bistatic wind measurements from these instruments at four locations east of Poker Flat showed good agreement with collocated monostatic and bistatic wind estimates from the two SDI's. Since the two arrays utilized different instruments (with different optics, fields-of-view, spectral derivation and analysis), the high level of agreement provides a completely independent validation of the analysis technique. This comparison will be the focus of a future article.

4.2. January 20, 2010

[41] Figure 8 displays the monostatic and bistatic wind results from the night of January 20, 2010. Frames in this figure are displayed at a nominal time resolution of 4 min, and span approximately 40 min of local time (in the magnetic dawn sector) beginning at 1634 UT (approximately 0450 MLT). The format is identical to Figure 7 although the time resolution is much higher. Agreement between the station monostatic fits was very good throughout this period, and bistatic wind estimates were also in close agreement with the monostatic wind fields. Note that the bistatic fit is based solely on line-of-sight data from the two instruments, and makes no use of monostatic fit results. In addition, bistatic coverage was very good on both sides of the Gakona/Poker Flat great circle.

[42] At the beginning of this sequence of frames, the wind field showed a smooth spatial transition from approximately sunward flow in the magnetic north to magnetic southwestward flow in the magnetic south. During the succeeding 40 minutes the sunward flow in the north increased in magnitude while the southwestward flow in the south remained relatively constant. The intensification of the sunward flow occurred as an auroral arc moved into the magnetic north of the Poker Flat field-of-view. This arc was accompanied by strong perturbations in the horizontal component of the geomagnetic field measured at Fort Yukon (66.56N, 145.22W), with ΔH decreasing from −100 nT to −460 nT between 1600 and 1750 UT. These indicators strongly suggest that momentum transfer from convecting ions was responsible for the sunward wind acceleration. By

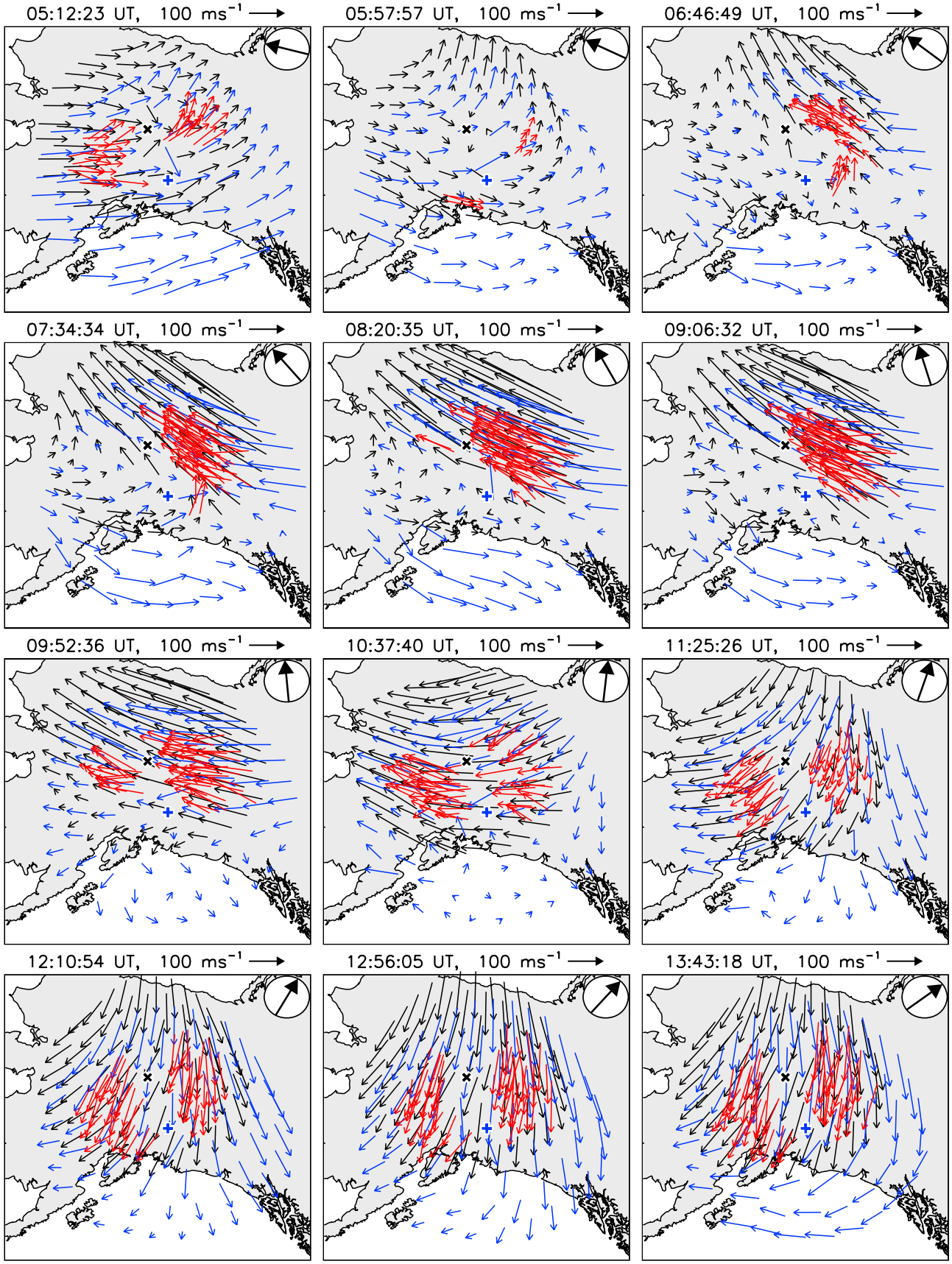

Figure 7. Monostatic and bistatic wind fields on January 24, 2010, between 0512–1343 UT (1727–0158 MLT). Plot format is the same as Figure 6.

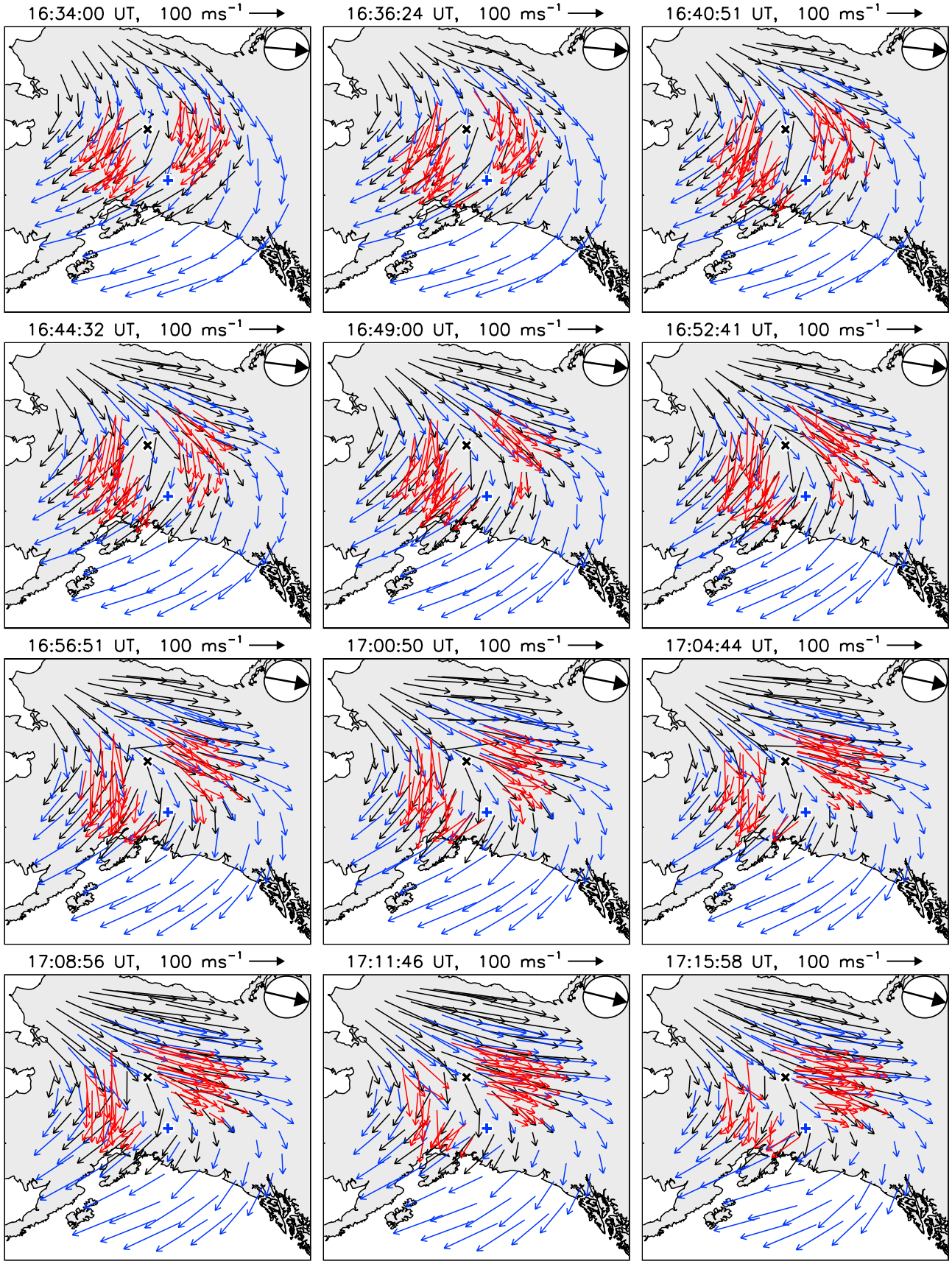

Figure 8. Monostatic and bistatic wind fields on January 20, 2010, between 1634–1715 UT (0450–0530 MLT). Plot format is the same as Figure 6.

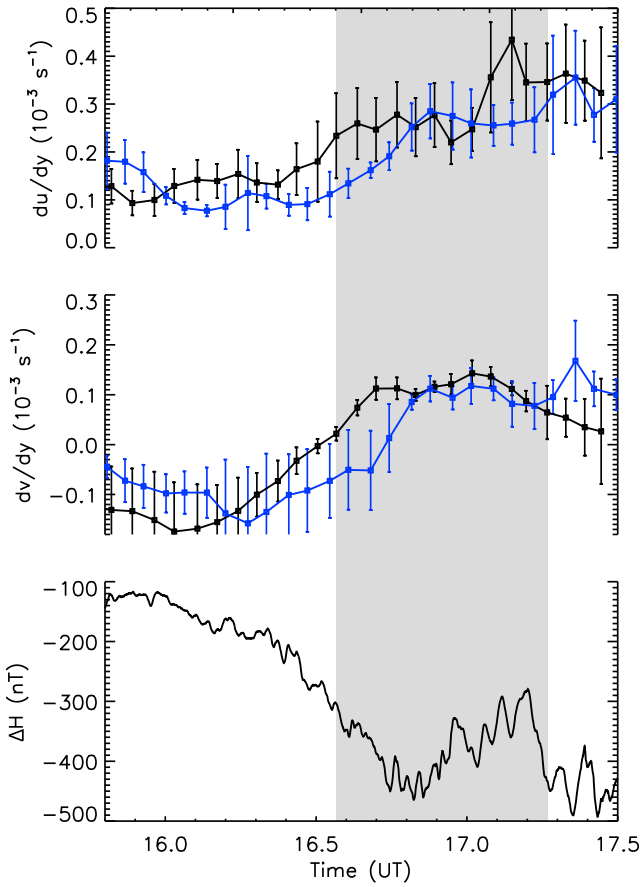

Figure 9. (top) Meridional gradient of the zonal wind, averaged across the Poker Flat (black curve) and Gakona (blue curve) fields-of-view. 'Error-bars' indicate the 1σ spread in the gradients estimates in each ring. (middle) Meridional gradient of the meridional wind, with colors and error-bars as in Figure 9 (top). (bottom) Changes in the horizontal component of the geomagnetic field relative to the median of that component over the entire night, measured from Fort Yukon (66.56N, 145.22W). Grey shaded area indicates the time range displayed in Figure 8.

1715 UT, this acceleration had produced a wind field that was much more strongly sheared and divergent in the magnetic meridional direction, relative to the start of the period.

[43] In Figure 9 are shown the estimates of meridional shear ($\partial u/\partial y$ (Figure 9, top)), meridional divergence ($\partial v/\partial y$ (Figure 9, middle)) and the change in the H component of the magnetic field as measured at Fort Yukon (ΔH, (Figure 9, bottom)). The gradient estimates were obtained from the monostatic wind fit described in section 3.2. One gradient estimate was obtained for each ring which contained six or more zones (therefore all rings excluding the central zone). The error-bars in the first and second panels of Figure 9 thus represent the $\pm 1\sigma$ width in gradient estimates across all rings from which these estimates were obtained. The grey shaded area indicates the time period displayed in Figure 8.

[44] Spatial gradients in the neutral thermosphere play an important role in the momentum balance at high-latitudes as they are opposed by viscosity. They can therefore remain appreciable even in the absence of local acceleration due for example to ion drag. The increase in the meridional shear gradient and divergence gradient (Figure 9, first and second panels) clearly tracked the decrease in ΔH (Figure 9, bottom). The time-lag between the response of the Poker Flat and Gakona divergence estimates is likely a consequence of both the differing locations and differing size and geographical projections of the instrument fields-of-view. Monostatic divergence/shear estimates are derived from an entire ring of line-of-sight observations. The Poker Flat field-of-view, being smaller, allowed a more rapid response in the spatially averaged gradients, and would more easily support large gradients (less area over which to average). In addition, the Poker Flat field-of-view was closer (in this case) to the enhanced sunward flow in the magnetic north which drove the shear and divergence.

4.3. September 21, 2010

[45] Data from September 21, 2010 are shown in Figure 10. These data span approximately 3.5 hours in the pre-magnetic midnight dusk sector, beginning at 0658 UT (~1915 MLT), and are displayed at a nominal time resolution of 18 min (again much lower than the raw sample frequency). Bistatic coverage was generally good throughout the period displayed, however coverage in the magnetic west was reduced from 0917 UT onwards.

[46] The first three frames in Figure 10 show strong sunward flow in the magnetic north and a region of magnetic southward flow in the magnetic south. In a sunward/anti-sunward sense, the flow characteristics depicted in these three frames were similar to those seen in the last three frames from January 20, 2010 (Figure 8). The region of sunward flow on September 21 spanned a larger range of magnetic latitudes than in the data from January 20. Also, the geographic east-west directions of the flow were opposite on these two nights, as the January 20 data were recorded in the magnetic dawn sector, while the data from September 21 were recorded in the pre-magnetic midnight dusk sector.

[47] Agreement between the monostatic wind estimates in the region magnetically south of the Gakona/Poker Flat great circle was relatively poor in the first frame of Figure 10, and the bistatic wind estimates showed better agreement with the monostatic winds derived from Gakona than those from Poker Flat at that time. Agreement between all three sets of wind estimates had improved by 0737 UT, at which time the southward flow in the magnetic south had decreased in magnitude, and was beginning to rotate toward the sunward direction. By 0821 UT the wind field was relatively uniform across the combined instrument field-of-view, however there were regions of disagreement between monostatic wind fields, particularly in the magnetic north and west, where Gakona wind estimates had a consistently larger southward component compared to estimates from Poker Flat. In both of these regions the bistatic wind estimates were generally in agreement with winds from the Gakona SDI.

[48] Between 0840–0859 UT the stations began to move into a transition region characterized by westward flow in the west and eastward flow in the east. Entry into this transition region was marked by the very low wind speeds at the magnetic eastward edge of the Gakona field-of-view at 0840 UT. Divergent flow was then apparent in the wind fields from 0859–0957 UT. Monostatic consistency was

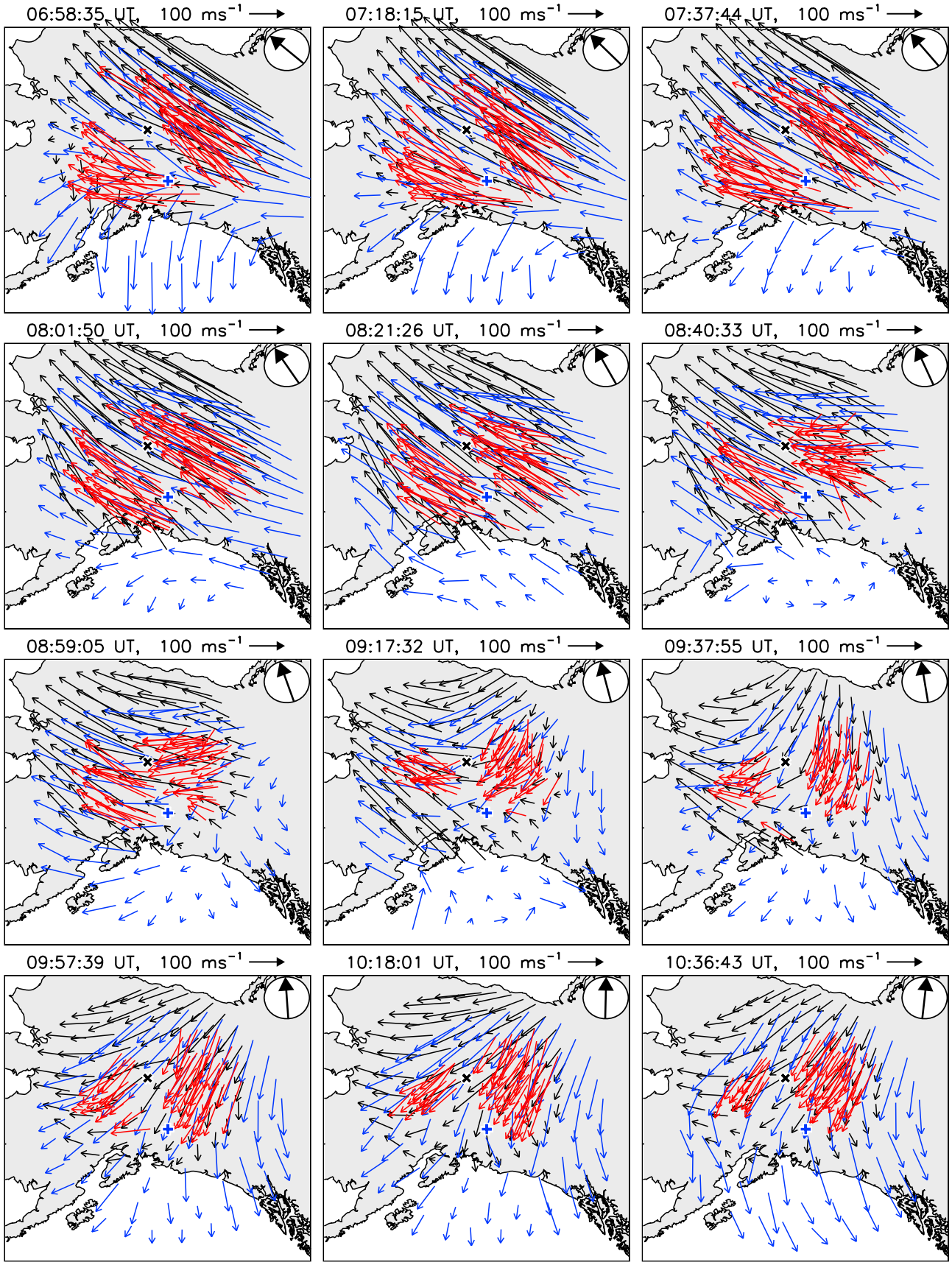

Figure 10. Monostatic and bistatic wind fields on September 21, 2010, between 0658–1036 UT (1913–2251 MLT). Plot format is the same as Figure 6.

generally good during this period (0859–0957 UT), however there was a small region magnetically west of Gakona in which winds estimated from Gakona were directed magnetic southward, while the bistatic and Poker Flat monostatic winds were directed magnetic westward.

[49] In the last three frames there was again some disagreement between the Gakona and Poker Flat monostatic wind estimates at the magnetic westward edge of the Gakona field-of-view, where Gakona wind estimates were magnetic southward while Poker Flat estimates were directed southwestward. The disagreement was particularly noticeable in the last frame at 1036 UT, where the monostatic wind fields derived from each instrument showed curvature in opposite directions. In these cases the bistatic winds tended to support the Gakona-derived wind fields, rather than those derived from Poker Flat.

5. Discussion

[50] The three nights presented above demonstrate characteristics of the thermospheric neutral wind fields that are often observed above Alaska during periods of enhanced geomagnetic activity. All three nights displayed instances of sheared flow, driven by sunward winds in the magnetic north, and generally associated with optical aurora and magnetic field perturbations on the ground (as for example in Figure 9). Similar observations were presented by *Conde et al.* [2001], using data from the Poker Flat SDI. There were also periods during which the wind fields displayed curvature (1634 UT on January 20 and 1343 UT on January 24, for example) and divergence (1125 UT on January 24, 0957 UT on September 21). Again, these types of wind fields have been reported previously [e.g., *Conde and Smith*, 1998].

[51] The derivation of the monostatic wind fields presented here relied on the assumptions outlined in section 3.2, most notably on the first-order Taylor approximation and the assumption that the zonal gradient of the meridional wind was zero in magnetic coordinates. The 'big picture' view of the wind fields derived in this way was generally consistent with the behavior that would be expected of thermospheric winds after taking into account the dominant driving forces such as ion drag and the solar pressure gradient. However, it has not until now been possible to determine to what degree the monostatic wind fields are limited by these assumptions in their ability to accurately represent the wind behavior at smaller scales.

[52] Figure 11 shows time series of the field-of-view average geographic zonal and meridional wind components inferred monostatically from each instrument (Poker Flat in black, Gakona in blue) for the 19 days analyzed thus far. Also shown in orange are the wind components output by the 1993 Horizontal Wind Model (HWM93) [see *Hedin et al.*, 1991] for comparison. HWM93 output was generated using the appropriate geophysical conditions for each night (as an example of these conditions, daily mean Ap is shown at the right of Figure 11).

[53] The monostatic vector wind comparisons shown in Figures 7, 8, and 10, along with the average winds presented in Figure 11, demonstrate that for the majority of the time the independently derived monostatic wind fields from the two instruments are in very good agreement with each other. Driven as it is by the planetary average geomagnetic indices (daily mean Ap and 3-hour *ap*), HWM93 was often unable to reproduce any but the most general trends in the observed wind flow. This is not surprising at auroral latitudes where wind flows are often strongly and locally perturbed by the dynamic auroral oval.

[54] Differences in average wind components between the two instruments can arise due to the different locations of the two instruments, particularly in relation to the auroral oval, which often introduces strong shear into the observed wind fields (as demonstrated in all three monostatic/bistatic comparison figures). These differences, while interesting in the context of small-scale variability, do not greatly affect the large-scale interpretation of the wind flow, which for much of the time shows very good agreement between the two instruments.

[55] This suggests that the assumptions underlying the vector wind fit are reasonable, even during periods when local driving forces vary rapidly with time and produce strong spatial gradients. However, significant differences between monostatic wind estimates from the two stations are sometimes observed over limited areas, as for example in the last two frames in Figure 10. Again, these differences in vector direction and magnitude are often relatively small, and do not greatly affect the large-scale interpretation of the wind flow, however it is necessary to understand why the differences do occur, in order to gain some insight into the validity of the vector fit assumptions.

[56] Poor data quality (due for example to localized cloud along a given line-of-sight, or one-off measurement artifacts) is one reason why monostatic estimates in common-volumes may differ, and is perhaps the most obvious. A second possibility may be due to a variation in the peak airglow emission altitude due to auroral precipitation, which may reduce the peak emission height by up to $\sim$60 km compared to the case where no aurora are present [e.g., *Sica et al.*, 1986]. Under these conditions the two instruments may no longer be sampling a common region of the sky. This combined with appreciable vertical gradients in the horizontal winds could produce inconsistent estimates between the two instruments. A third possibility is that one or more of the assumptions underlying the vector fit preclude the instruments from inferring wind fields which accurately represent the real wind flow everywhere within their field-of-view.

[57] Consider Figure 12, where three composite wind fields are shown from April 2, 2010. The top row of panels shows the large-scale view of the wind fields in the same format as Figures 7–10, while the bottom row shows the same fields with the view zoomed-in to cover the region outlined by the solid lines in upper images. Each frame is separated in time by approximately 10 min. The first frame (first panel, 0947 UT), shows a (comparatively) large discrepancy between the Poker Flat and Gakona derived monostatic wind fields. While both monostatic fields indicated curved flow from antisunward in the magnetic north to magnetic southwestward in the magnetic south, the wind field derived from Poker Flat suggested a greater curvature than did the field derived from Gakona.

[58] This discrepancy was most pronounced magnetically south and southwest of the Gakona/Poker Flat great circle (the area outlined by the solid black lines in the upper images). Focusing on the region of bistatic overlap (Figure 12,

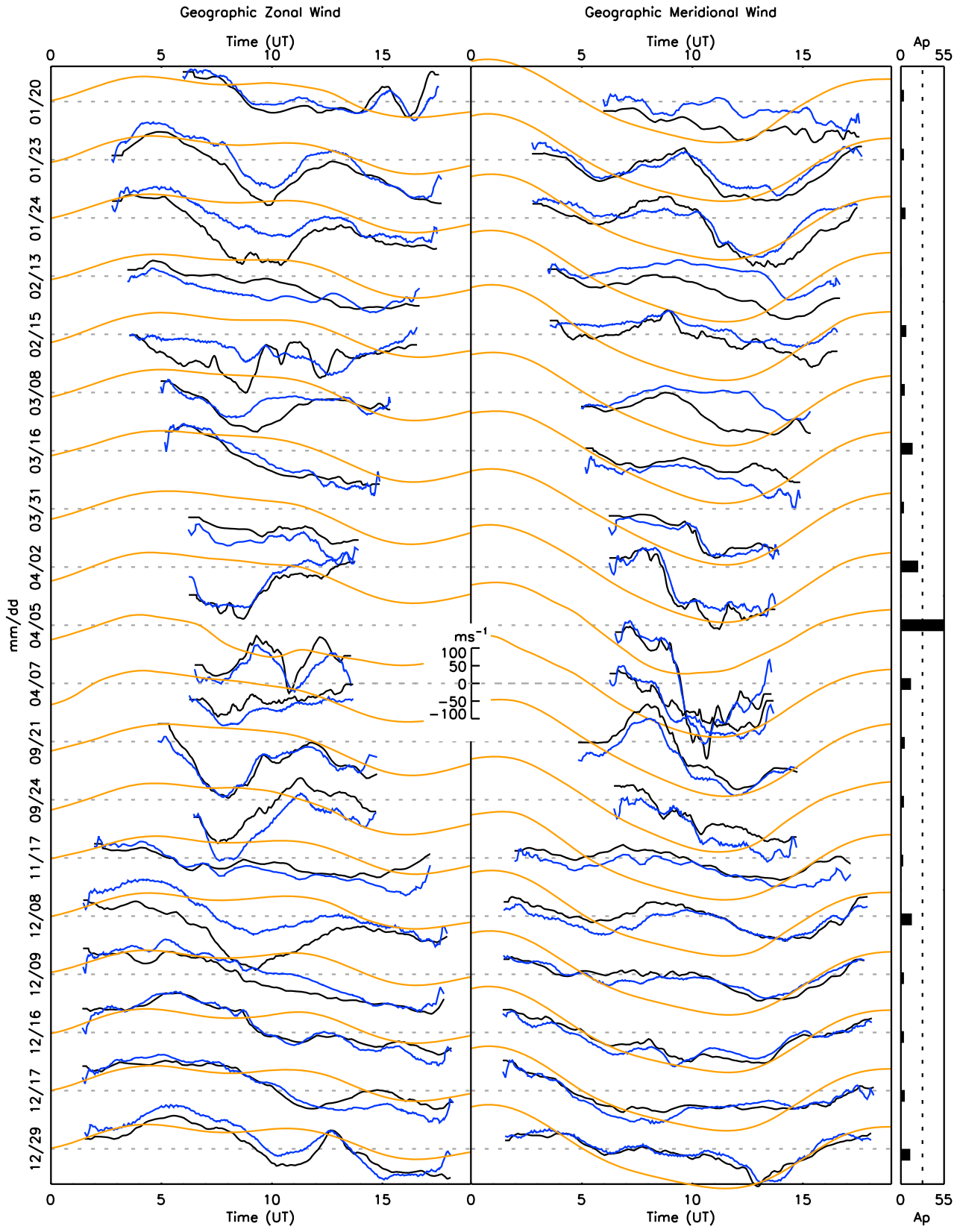

Figure 11. All-sky average geographic wind components inferred from Poker Flat (black) and Gakona (blue), with 1993 Horizontal Wind Model (HWM) estimates overlaid in orange. Zonal wind is displayed in the left column, and meridional wind is displayed in the right column. The vertical wind scale is shown in the middle of the figure, and the daily mean Ap value used to generate the HWM output shown at the right edge of the figure (two other geophysical inputs to HWM, 3-hour *ap* and $F_{10.7}$, are not shown).

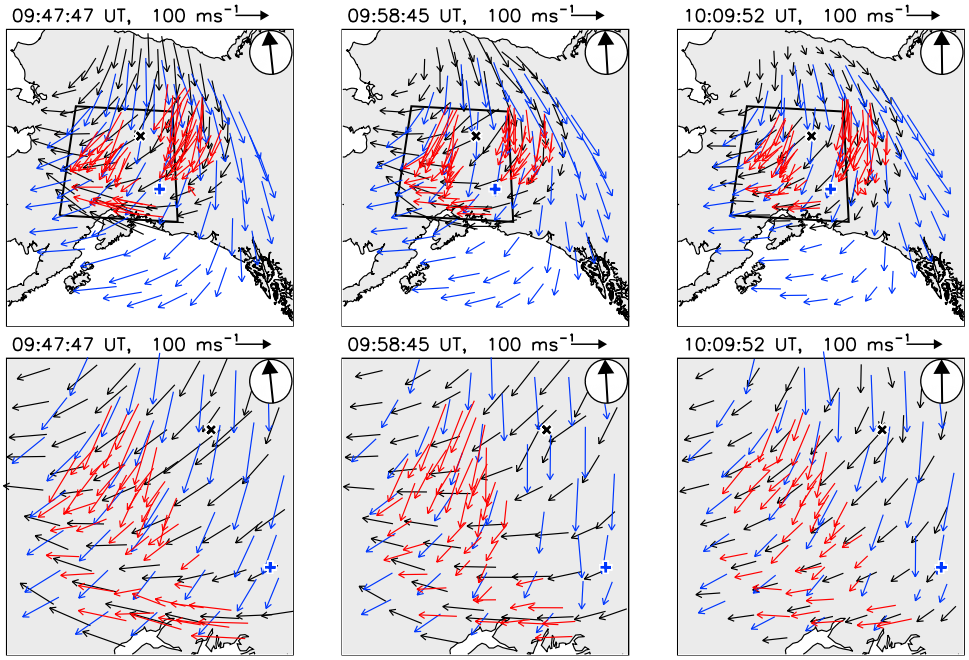

Figure 12. Example of discrepancy between monostatic wind estimates, from data recorded on April 2, 2010. (top) Large-scale view, same format as Figures 7–10. (bottom) Small-scale view, zoomed-in to the area outlined by the solid lines in upper panels.

bottom), the monostatic winds from Poker Flat were rotated toward the magnetic west relative to the Gakona wind estimates everywhere in this region. The bistatic estimates indicated that neither of the monostatic wind fields were entirely accurate everywhere in the region. Instead, the bistatic winds were more properly aligned with the Gakona estimates at the magnetic westward edge (toward the upper left corner of the figure panels) and with the Poker Flat estimates toward the magnetic southeastward edge (toward the lower edge of the figure panels).

[59] Approximately twenty minutes after the first displayed frame, the two monostatic wind fields were in much closer agreement, both with each other and with the bistatic wind estimates. Note however that the bistatic estimates did not change direction significantly during this time, but remained relatively constant. The improvement in consistency between the three types of wind estimates was due predominantly to the rotation of the monostatic estimates from each instrument, southward in the case of Poker Flat, and westward in the case of Gakona. It is therefore reasonable to conclude that the bistatic estimates were the most accurate in all three frames, and that the two monostatic wind fields, for whatever reason, were unable to model the winds accurately in this region. Note also that the monostatic wind estimates were generally in good agreement in the region magnetically northward of the Gakona/Poker Flat great circle. This likely implies that the all-sky averaged first-order gradients were not able to capture the full variation of the wind field everywhere within the field-of-view.

[60] Of course it is not surprising that the bistatic wind estimates should be more accurate than the fitted monostatic wind estimates in this particular case. The only assumption (beyond that of viewing a common-volume) required to generate a bistatic horizontal wind estimate is that of the local vertical wind magnitude (in this case assumed to be zero). Given the frequently small magnitude (± 30 ms^{-1} [see, e.g., *Conde and Dyson*, 1995]) of thermospheric vertical winds, and the applied geometrical filtering ($\eta > \pi/6$), this should represent only a small correction most of the time. Thus bistatic estimates are much closer to a direct measurement of the *local* horizontal wind than those inferred from the azimuthal variation of radial line-of-sight measurements, as is done for the monostatic winds.

[61] Without an independent trusted measurement of the true wind field (e.g. from in-situ measurements such as TMA chemical releases) it is not possible to quantify the degree to which bistatic estimates 'improve' over monostatic ones. However, it is reasonable to assume that the bistatic estimates are often 'closer' to the true wind field than are the monostatic estimates due to the far less restrictive assumptions underlying the bistatic technique. The example in Figure 12 shows that although the monostatic wind fields are often very consistent with each other over large spatial scales, there are times when these fields may not accurately estimate the flow at small scales or in localized regions. In any application where one needs to be sure that the wind is accurately measured at small scales it would be important to use bistatic or tristatic geometry.

[62] To quantify the level of agreement between the station monostatic wind estimates and the bistatic estimates, the monostatic wind estimates from each station have been spatially interpolated to the bistatic locations, and the vector difference (speed and direction/angle) calculated. These results are shown in the first and second panels of Figure 13, for the night of January 24, 2010. At each time, the median vector difference was calculated over all available bistatic locations (filtered by geometry and wind component uncertainty, as described at the beginning of section 4), and

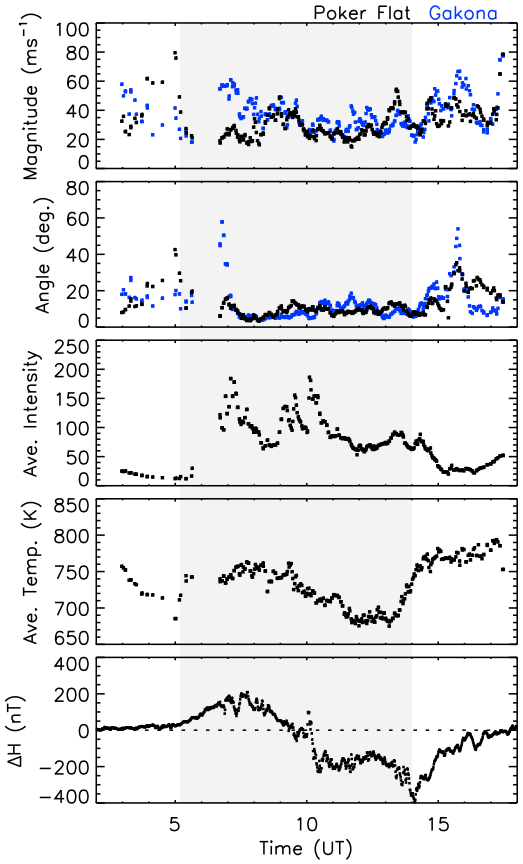

Figure 13. First and second panels show median difference between station monostatic (Poker Flat, black; Gakona, blue) and bistatic estimates on January 24, 2010, wind speed in the first panel and direction in the second panel from the top. The third panel shows median intensity across bistatic locations. The fourth panel shows median temperature across bistatic locations, and the fifth panel displays ΔH as measured from Fort Yukon. Mean 1σ widths of the distributions of each data point over the whole night were wind magnitude 22 ms^{-1}, wind direction 14 degrees, temperature 25 K.

plotted as a single point (black for Poker Flat, blue for Gakona). Each point therefore indicates the median difference in either vector magnitude (wind speed, first panel) or direction (second panel) between the monostatic wind estimates from each station and the bistatic wind estimates, across all available bistatic estimates at each common time. In the third and fourth panels of Figure 13 are shown the median intensity and temperature averaged across the bistatic locations (and averaged between station estimates at the bistatic locations), and beneath them (fifth panel) is shown the change in the H component of the geomagnetic field as measured from Fort Yukon.

[63] The first panel of Figure 13 shows that the median difference in wind speed between the monostatic and bistatic estimates was generally greater than 20 ms^{-1}, typically around 30–40 ms^{-1}. It also shows that neither of the instruments was consistently in closer agreement with the bistatic results than the other. Instead, at times Gakona differences were smaller (1300–1400 UT for example), while at other times the Poker Flat differences were smaller (0700–0800 UT). The difference in vector direction (second panel) shows a similar result. For the majority of the time the monostatic wind vectors were directed within 20° of the bistatic vectors, and were often within 10°, and neither instrument showed consistently better agreement than the other.

[64] Note that since the monostatic and bistatic analysis techniques are very different, we would expect the magnitude of the vector difference to be greater than zero due solely to the presence of noise. The absence of any systematic behavior in these differences likely indicates a substantial contribution due to noise. No strong correlation was observed between the magnitude of the vector differences (in speed or direction) and parameters such as average temperature or intensity, or the magnitude of ΔH. There was also no significant correlation with instrumental parameters (not shown) such as average signal-to-noise ratio, average spectral fit reduced chi-squared, or average line-of-sight wind uncertainty. This result is typical of the data that have been analyzed thus far, and suggests that the validity of the monostatic technique is not simply related to any obvious instrumental or geophysical parameter.

6. Conclusion

[65] In this article we have presented, for the first time, a comparison between monostatic wind fields inferred from two scanning Doppler imagers viewing a substantial thermospheric common-volume. These comparisons have demonstrated the often very good agreement between the independently derived monostatic wind fields, as well as the ability of these SDI's to easily resolve the large-scale behavior of the neutral horizontal wind field and to reasonably infer the small-scale behavior most of the time. We have also shown that, at certain times, the monostatic wind fields can contain artifacts which do not appear to accurately characterize the small-scale or localized wind flow. This is not surprising given the nature of the assumptions underlying the monostatic wind fit.

[66] In order to truly resolve the small-scale behavior of the wind field, more direct measurements are needed. We have presented wind estimates generated from bistatic inversion of common-volume line-of-sight wind measurements from both the Gakona and Poker Flat SDI's. The high spatial resolution of these two instruments allowed for bistatic inversion at approximately 75 locations (after filtering by viewing geometry) across the region of overlap of their fields-of-view. From these bistatic inversions we estimated horizontal wind vectors by assuming zero local vertical wind.

[67] Comparison of collocated monostatic and bistatic wind estimates revealed generally very good agreement. While the types of wind structures observed in this work have been reported previously, we now have far more confidence in the accuracy of these fields, given that the bistatic wind estimates produce very similar results, without the assumptions required for the monostatic fit. While these results indicate that the assumptions underlying the monostatic wind fit are reasonable under a large range of geophysical conditions, there were times when the monostatic

wind fields were clearly unable to accurately represent the wind flow at all locations within their fields-of-view.

[68] It is therefore important to note that for applications requiring accurate knowledge of the small-scale wind structure, it is essential to remove as many assumptions as possible, and in these cases bistatic (or tristatic) observations are required. For example, studies have shown that the electric field spatial variability can have a significant impact on the estimated rate of Joule heating [*Codrescu et al.*, 1995; *Deng and Ridley*, 2007]. The calculation of Joule heating also relies on the neutral wind [see, e.g., *Thayer and Semeter*, 2004; *Aruliah et al.*, 2005]. Given that the neutral wind field can also show significant spatial variability [e.g., *Conde and Smith*, 1998; *Conde et al.*, 2001], bistatic/tristatic neutral wind sampling would be critical for accurate estimates of Joule heating. Gravity wave studies are another obvious area in which bistatic/tristatic neutral wind measurements would be highly desirable.

[69] The capability to image a common thermospheric volume using two SDI's, and thereby deduce horizontal wind estimates with minimal assumptions, represents a big step forward in our ability to accurately resolve small-scale thermospheric dynamics. In two future papers, we will use these bistatic data to investigate the behavior of the vertical wind field and horizontal wind gradients.

[70] **Acknowledgments.** Gakona SDI installation and operations were supported by Carl Andersen, Tim Manning and Marty Karjala. Poker Flat SDI operations were supported by Carl Andersen, Don Hampton and Brian Lawson. The authors gratefully acknowledge the assistance provided by these individuals.

[71] Robert Lysak thanks the reviewers for their assistance in evaluating this paper.

References

Anderson, C., M. Conde, P. Dyson, T. Davies, and M. J. Kosch (2009), Thermospheric winds and temperatures above Mawson, Antarctica, observed with an all-sky imaging, Fabry-Perot spectrometer, *Ann. Geophys.*, *27*, 2225–2235.

Anderson, C., T. Davies, M. Conde, P. Dyson, and M. J. Kosch (2011), Spatial sampling of the thermospheric vertical wind field at auroral latitudes, *J. Geophys. Res.*, *116*, A06320, doi:10.1029/2011JA016485.

Aruliah, A. L., and D. Rees (1995), The trouble with thermospheric vertical winds: geomagnetic, seasonal and solar cycle dependence at high latitudes, *J. Atmos. Terr. Phys.*, *57*(6), 597–609.

Aruliah, A. L., E. M. Griffin, I. McWhirter, A. D. Aylward, E. A. K. Ford, A. Charalambous, M. J. Kosch, C. J. Davis, and V. S. C. Howells (2004), First tristatic studies of meso-scale ion-neutral dynamics and energetics in the hight-latitude upper atmosphere using collocated FPIs and EISCAT radar, *Geophys. Res. Lett.*, *31*, L03802, doi:10.1029/2003GL018469.

Aruliah, A. L., E. M. Griffin, A. D. Aylward, E. A. K. Ford, M. J. Kosch, C. J. Davis, V. S. C. Howells, S. E. Pryse, H. R. Middleton, and J. Jussila (2005), First direct evidence of meso-scale variability on ion-neutral dynamics using co-located tristatic FPIs and EISCAT radar in Northern Scandinavia, *Ann. Geophys.*, *23*, 147–162.

Aruliah, A. L., E. M. Griffin, H.-C. I. Yiu, I. McWhirter, and A. Charalambous (2010), SCANDI–an all-sky Doppler imager for studies of thermospheric spatial structure, *Ann. Geophys.*, *28*, 549–567.

Browning, K. A., and R. Wexler (1968), The determination of kinematic properties of a wind field using Doppler radar, *J. Appl. Meteorol.*, *7*, 105–113.

Burnside, R. G., F. A. Herrero, J. W. Meriwether Jr., and J. C. G. Walker (1981), Optical observations of thermospheric dynamics at Arecibo, *J. Geophys. Res.*, *86*(A7), 5532–5540.

Codrescu, M. V., T. J. Fuller-Rowell, and J. C. Foster (1995), On the importance of *E*-field variability for Joule heating in the high-latitude thermosphere, *Geophys. Res. Lett.*, *22*(17), 2393–2396, doi:doi:10.1029/95GL01909.

Conde, M. (2001), Analysis of Fabry-Perot spectra of lidar backscatter echoes, in *ANARE Reports*, vol. 146, edited by R. J. Morris and P. J. Wilkinson, pp. 91–114, Antarct. Div., N. S. W., Australia.

Conde, M., and P. L. Dyson (1995), Thermospheric vertical winds above Mawson, Antarctica, *J. Atmos. Terr. Phys.*, *57*(6), 589–596.

Conde, M., and R. W. Smith (1995), Mapping thermospheric winds in the auroral zone, *Geophys. Res. Lett.*, *22*(22), 3019–3022.

Conde, M., and R. W. Smith (1997), 'Phase compensation' of a separation scanned, all-sky imaging Fabry-Perot spectrometer for auroral studies, *Appl. Opt.*, *36*, 5441–5450.

Conde, M., and R. W. Smith (1998), Spatial structure in the thermospheric horizontal wind above Poker Flat, Alaska, during solar minimum, *J. Geophys. Res.*, *103*(A5), 9449–9472.

Conde, M., et al. (2001), Assimilated observations of thermospheric winds, the aurora, and ionospheric currents over alaska, *J. Geophys. Res.*, *106*(A6), 10,493–10,508.

Deng, Y., and A. J. Ridley (2007), Possible reasons for underestimating Joule heating in global models: *E* field variability, spatial resolution, and vertical velocity, *J. Geophys. Res.*, *112*, A09308, doi:10.1029/2006JA012006.

Ford, E. A. K., A. L. Aruliah, E. M. Griffin, and I. McWhirter (2006), Thermospheric gravity waves in Fabry-Perot interferometer measurements of the 630.0 nm OI line, *Ann. Geophys.*, *24*, 555–566.

Ford, E. A. K., A. L. Aruliah, E. M. Griffin, and I. McWhirter (2008), Satistical analysis of thermospheric gravity waves from Fabry-Perot interferometer measurements of atomic oxygen, *Ann. Geophys.*, *26*, 29–45.

Greet, P. A., J. L. Innis, and P. L. Dyson (2002), Thermospheric vertical winds in the auroral oval/polar cap region, *Ann. Geophys.*, *20*, 1987–2001.

Griffin, E. M., A. L. Aruliah, I. McWhirter, H.-C. I. Yiu, A. Charalambous, and I. McCrea (2008), Upper thermospheric neutral wind and temperature measurements from an extended spatial field, *Ann. Geophys.*, *26*, 2649–2655.

Hedin, A. E., et al. (1991), Revised global model of thermosphere winds using satellite and ground-based observations, *J. Geophys. Res.*, *96*(A5), 7657–7688.

Jarrett, A. H., and M. J. Hoey (1966), Observations of the 6300 Å OI nightglow emission, *J. Atmos. Terr. Phys.*, *28*, 175–183.

Meriwether, J. W., M. F. Larsen, R. Hedden, and M. Faivre (2006), Measuring thermospheric winds and temperatures with a tri-static Fabry-Perot interferometer network in Alaska, *Eos Trans. AGU*, *87*(52), Fall Meet. Suppl., Abstract SMD21D-06.

Roble, R. G., P. B. Hays, and A. F. Nagy (1968), Calculated [OI] 6300 Å nightglow Doppler temperatures for solar cycle minimum, *Planet. Space Sci.*, *16*(9), 1109–1113.

Sica, R. J., M. H. Rees, R. G. Roble, G. Hernandez, and G. J. Romick (1986), The altitude region sampled by ground-based Doppler temperature measurements of the OI 15867 K emission line in aurorae, *Planet. Space Sci.*, *34*(5), 483–488.

Sipler, D. P., M. A. Biondi, and M. E. Zipf (1995), Vertical winds in the midlatitude thermosphere from Fabry-Perot interferometer measurements, *J. Atmos. Terr. Phys.*, *57*(6), 621–629.

Thayer, J. P., and J. Semeter (2004), The convergence of magnetospheric energy flux in the polar atmosphere, *J. Atmos. Sol. Terr. Phys.*, *66*(10), 807–824.

Wark, D. Q. (1960), Doppler widths of the atomic oxygen lines in the airglow, *Astrophys. J.* , *131*, 491–501.

C. Anderson and M. Conde, Geophysical Institute, University of Alaska Fairbanks, Fairbanks, AK 99775, USA. (callum@gi.alaska.edu)

M. G. McHarg, Physics Department, U.S. Air Force Academy, 2354 Fairchild Hall, Ste. 2A31, Colorado Springs, CO 80840, USA.